PHYSICAL REVIEW B **96**, 020506(R) (2017)

Evidence for enhanced phase fluctuations in nanostructured niobium thin films

Ting-Hui Chen, Hsiang-Hsi Kung, Chang-Ran Wang, Chia-Tso Hsieh, and Wei-Li Lee*
Institute of Physics, Academia Sinica, Nankang, Taipei 11529, Taiwan
(Received 4 November 2016; published 24 July 2017)

In a superconducting nanostructure, phase fluctuations are prominent and give rise to finite resistance below superconducting transition temperature T_c. By using a monolayer polymer/nanosphere hybrid we developed previously, we fabricated a large array of interconnected niobium (Nb) honeycomb lattices with the thinnest interconnected linewidth d ranging from 36 nm to 89 nm. The honeycomb cells form a highly ordered triangular lattice with more than 10^8 unit cells extending over few mm^2 area, which enables the detailed transport study at nanometer scales. We found T_c gradually drops with decreasing d due to the phase-slip effect, while the critical field at lower temperature tends to follow that of a continuous Nb thin film. One likely scenario is to consider a model system of numerous superconducting islands interconnected by short phase-slip junctions, where the phase coherence is dictated by the phase slippage in the nanoconstriction. This was strongly supported by the excellent fitting to the thermally activated phase-slip model and also the unusual phenomena of transition width narrowing in high fields.

DOI: 10.1103/PhysRevB.96.020506

In the high-T_c cuprates and some organic superconductors where phase rigidity is weak despite the large binding energy, a host of experiments have uncovered a vortex-liquid state that extends high above the critical Meissner transition temperature [1–3]. On the other hand, in the low-T_c superconductors, the onset of diamagnetism is very well described by the mean-field BCS description [4,5]. The main factor is the large Cooper-pair density, which leads to a phase rigidity of the pair condensate that is extremely stiff even very close to the critical transition temperature T_c. A consequence of this extreme stiffness is the strong suppression of phase fluctuations, which often precludes the observation of fluctuation phenomena arising from competition between superconductivity and other states. One way to tune the phase rigidity in a superconductor is by the phase slip mechanism. It has been demonstrated that the suppression of T_c in a single superconducting nanowire is driven by phase slips [6,7]. The unbinding of vortex-antivortex pairs in ultrathin superconducting films has also been investigated to test the Berezinskii-Kosterlitz-Thouless (BKT) theory [8–10].

Research on superconducting nanostructure goes back to the 1980s. The Little-Parks effect [11] was demonstrated in artificially nanopatterned superconducting films showing oscillatory behavior in resistance and magnetization under an applied magnetic field [12–16]. Josephson-junction arrays were also extensively studied to elucidate the BKT transition [17,18]. More recently, unusual insulator-superconductor transition [19] was observed in a nanohoneycomb array of holes in amorphous bismuth films demonstrating exotic Cooper pair localization effect. Here, we have exploited a recent advance to make interconnected Nb honeycomb lattice (INHL) with sub-100 nm nanostructures extending over 10^8 cells while still maintaining macroscopic correlation lengths, which is a rarely explored regime in terms of size and geometry compared to previous works. Our goal here is to exploit the long correlation length and the macroscopic size of our array to investigate the role of phase slip and rigidity in a low-T_c superconductor Nb. Unlike previous investigations [6,7,20], our INHL system shows richer phenomena arising from the interplay between the flux-line lattice and the phase fluctuations.

A series of INHLs with different interconnected linewidths d ranging from 36 nm to 89 nm was fabricated [21,22]. Figure 1(a) shows an SEM image of a Nb honeycomb lattice with separated islands, where red dotted lines indicate a single honeycomb cell with a size about 200 nm. For INHL with $d = 74$ nm, an atomic force microscope image taken by an ultrasharp tip is shown in Fig. 1(b). The cross-sectional depth profile along the dotted red line is given in the lower panel of Fig. 1(b) indicating a film thickness of $t = 34$ nm with a smooth edge profile. Figure 1(c) shows the temperature dependence of the normalized resistance R/R_n, where R_n is normal-state resistance at $T = 10$ K. The residual resistivity ratio (RRR), defined as $R(250\ \text{K})/R(10\ \text{K})$, progressively decreases with Nb linewidth d from RRR = 2.35 of a continuous Nb film to RRR = 1.26 with $d = 36$ nm, which suggests a reduced relative contribution from electron-phonon scattering as compared to impurity scattering in INHLs. The superconducting transition temperature T_c is defined as the temperature at which $R/R_n = 10^{-3}$. T_c equals 8.2 K in a continuous Nb thin film with a normal-state sheet resistance $R_\square(10\ \text{K}) = 2.096\Omega$. In the $d = 36$ nm sample, T_c drops to 5.13 K and $R_\square(10\ \text{K})$ increases by more than 20 folds to 53.4Ω. The d dependence of T_c is shown in Fig. 1(e), where the red dotted line refers to the T_c of a continuous Nb thin film. The inset figures of Fig. 1(e) are scanning electron microscopic (SEM) images with the white scale bars equal to 500 nm. The systematic decrease of T_c with d is also clearly shown in Fig. 1(d), which is a blowup view of the low T resistance transition to superconducting states. The error bar in d comes from the statistical average of more than 10 000 antidot diameters obtained from high resolution SEM images [22].

The sheet resistance $R_\square$ versus reduced field H/H_m of the $d = 36$ nm sample is shown in Fig. 2(a) at several temperatures slightly lower than $T_c = 5.13$ K, where H_m equals 600 Oe. A macroscopic nonzero $R_\square$ appears at noninteger H/H_m values

*wlee@phys.sinica.edu.tw

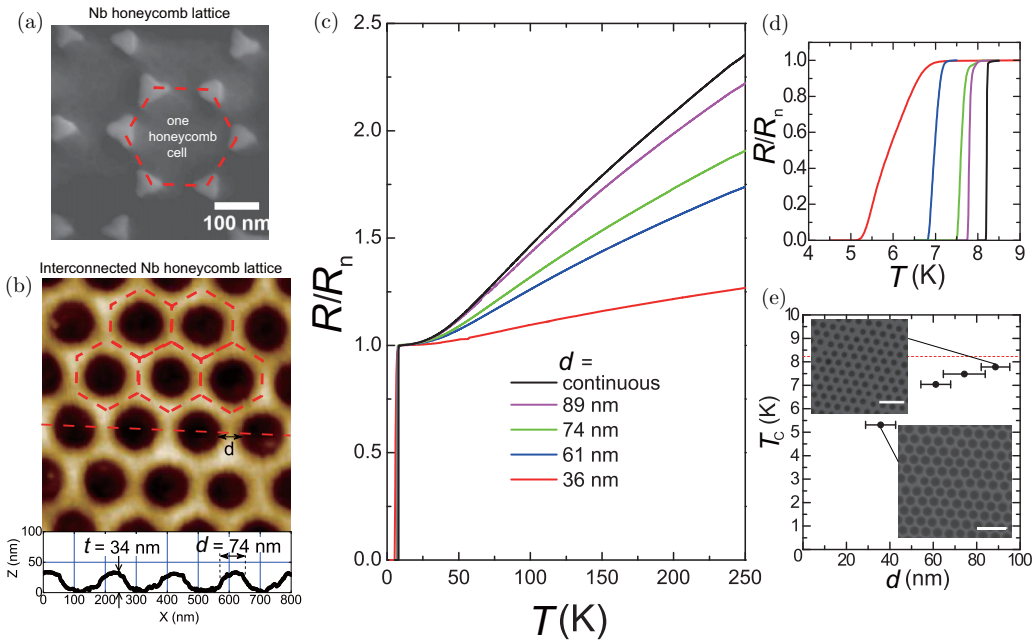

FIG. 1. (a) SEM image of a Nb honeycomb lattice with isolated Nb islands. The red dotted hexagon indicates a single cell of the lattice. (b) An AFM image of a interconnected Nb honeycomb lattice (INHL). The bottom panel shows the cross-sectional profile along the red dotted line showing a Nb thin film thickness $t \approx 34$ nm and interconnected linewidth $d \approx 74$ nm. (c) The normalized resistance R/R_n versus T for four INHL samples with different d's ranging from 36 nm to 89 nm. Low-T blowup view is shown in (d) that shares the same color code as (c). (e) The superconducting transition temperature T_c as a function of d. The upper and lower inset figures are SEM images for $d = 89$ and 36 nm, respectively, where the white scale bars equal 500 nm. The red dotted lines are the T_c value for a continuous Nb thin film. As d decreases, both the T_c and the residual resistivity ratio drops. The superconducting transition width is also getting wider for smaller d.

due to the kinetic energy loss from the induced screening supercurrents as expected from the Little-Parks effect [11], and $R_\square$ quickly reduces to zero at integer values of H/H_m and restores the zero resistance state. For an ideal triangular lattice with lattice spacing a, the matching field $H_m \equiv 2\Phi_0/\sqrt{3}a^2$, and $\Phi_0 \equiv h/2e$ is a fluxoid. We remark that the calculated $H_m = 598$ Oe ($a = 200$ nm) is nearly identical to our experimental $H_m = 600$ Oe obtained from the $R_\square$ oscillation shown in Fig. 2(a), which provides a strong support for the well-ordered nanostructures in our INHLs [22]. Figure 2(b) shows the contour plots of the normalized resistance R/R_n (color code) versus H/H_m and T for continuous Nb thin films and INHLs with $d = 36$ nm, 61 nm, and 89 nm. The blue and red regions represent the superconducting state and normal state, respectively. Apparent oscillations at the phase boundary were observed for all the INHLs, where the number of oscillation increases with decreasing d. The black line refers to $R/R_n(H,T) = 1/2$. We remark that the tuning of a single parameter d suppresses T_c by as much as 40% (8.2 to 5.13 K) without significantly affecting the curve of H_{c2} vs T particularly in low T and large H/H_m regime.

According to the Langer-Ambegaokar-McCumber-Halperin (LAMH) theory [23,24], the phase slip rate due to a fluxoid cutting across the nanowire is thermally activated over a free energy barrier $\Delta F(T) = (8\sqrt{2}/3)(H_C^2/8\pi)A\xi(T)$ corresponding to a superconducting condensation energy of a small volume $A\xi(T)$, where A is the cross-sectional area of the nanowire and $\xi(T)$ is the superconducting coherent length. A small current further breaks the balance between $+2\pi$ and -2π phase slips resulting in net phase changes and hence a finite resistance that can be described as

$$R_{\mathrm{LAMH}} = \frac{\pi\hbar^2\Omega}{2e^2k_BT}e^{-\Delta F(T)/k_BT}, \tag{1}$$

where the prefactor $\Omega \equiv (L/\xi)(\Delta F(T)/k_BT)^{1/2}(1/\tau_{GL})$, L is the length of the nanowire, and $\tau_{GL} = \pi\hbar/8k_B(T_c - T)$ is the characteristic relaxation time in Ginzburg-Landau theory. The temperature dependence of the resistance in INHLs with four different d's can be well fitted to the LAMH model using Eq. (1) shown as red lines in Fig. 3(a), where T_c and $\Delta F_0 \equiv \Delta F(T = 0\ \mathrm{K})$ are the only two fitting parameters. We remark that the excellent agreement between the LAMH fittings and experimental data points is obtained over a wide range of R/R_n from 0.1 to 10^{-7} extending over six orders of magnitude. The corresponding values of T_c and ΔF_0 as a function of d is plotted in Fig. 3(b), where the T_c from LAMH fittings (open red circles) shows systematic decrease with d consistent with that from the resistance data (solid black squares). On the other hand, the ΔF_0 from the LAMH fitting equals 10^5 K for $d = 89$ nm sample and drops linearly as d decreases giving $\Delta F_0 = 3900$ K for $d = 36$ nm. The linear fit (green line) to the ΔF_0 versus d data points is in accord with the LAMH model giving $\Delta F_0 \propto A = d \times t$ (cross-sectional area of the interconnected line). However, we note that it extrapolates linearly to a value of $d \approx 30$ nm as ΔF_0 goes to zero suggesting the failure of the LAMH model in small d regime. In a log scale as shown in Fig. 3(b), ΔF_0 can be better described by exponential decay

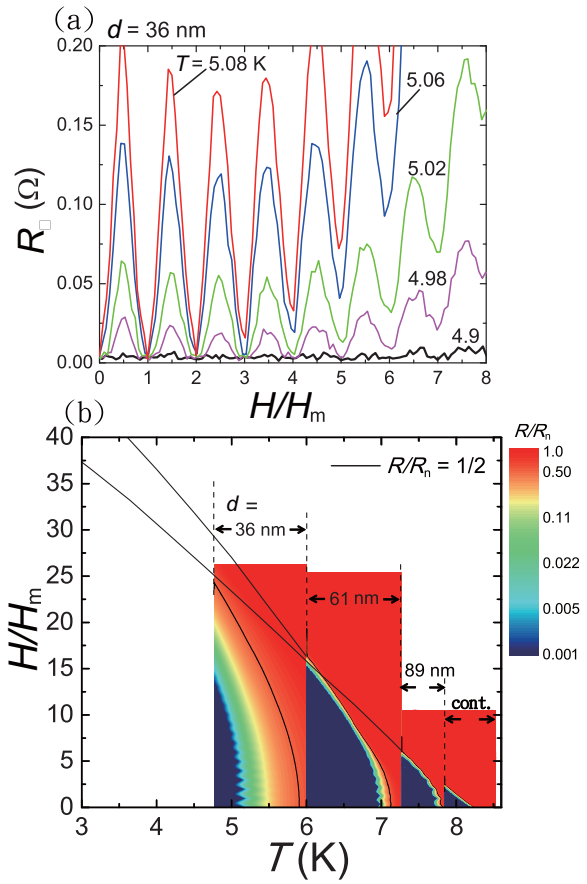

FIG. 2. (a) Sheet resistance $R_{\square}$ as a function of H/H_m for $d =$ 36 nm INHL close to T_c. The rapid and macroscopic increase of $R_{\square}$ at fractional values of H/H_m is a direct consequence of kinetic energy loss due to the screening supercurrents. (b) A phase diagram of INHL for continuous Nb film and $d = 36$ nm, 61 nm, and 89 nm. The color code represents the normalized resistance R/R_n, where red and blue regions refer to the normal state and the superconducting state, respectively. The solid black lines are the curves for $R/R_n = 0.5$. Apparent oscillations at the phase boundary were observed for all the INHLs.

(red dotted line) for $d \leqslant 60$ nm, where quantum phase slip effect may become more important [6,25].

Surprisingly, the broad transition width in INHL can be effectively suppressed by applying magnetic field H normal to the film surface as shown in Fig. 3(c), where the solid lines are the R/R_n versus T curves of $d = 61$ nm INHL sample at seven different H's ranging from zero to 6 kOe. The transition width ΔT_c, defined as the temperature difference between the two intercepts at $R/R_n = 0$ and 1 by linearly extrapolating the curve at $R/R_n = 0.5$ apparently drops from $\Delta T_c \approx 0.274$ K at $H = 0$ Oe (red curve) to $\Delta T_c \approx 0.063$ K at $H = 6$ kOe (black curve). The reduction of transition width in INHL is in big contrast to the continuous Nb thin film with the same film thickness shown as dotted lines sharing the same color codes as solid lines, where its ΔT_c only gradually increases with H. We remark that ΔT_c in INHL at high fields is nearly the same as that in the continuous Nb thin film at zero field. Figure 3(d) shows the normalized transition width $\Delta T_c/T_c$ versus magnetic field in four INHLs with different d values of 36 nm, 61 nm, 74 nm, and 89 nm. Two distinct regimes can be identified: phase-slip dominant regime and flux-creep dominant regime. In high H's, the magnetic fluxes inevitably penetrate the superconducting region of INHL and result in a larger $\Delta T_c/T_c$ with increasing H as expected by Anderson's flux-creep model [26]. On the other hand, in low field regime, the phase-slip effect plays an important role, and an unusual reduction of $\Delta T_c/T_c$ with increasing H was observed in all INHLs. The critical field H_x, at which the crossover from the phase-slip dominant to the flux-creep dominant regime occurs, increases rapidly as d drops. It gives $H_x \approx 3$ and 4 kOe for $d = 74$ and 61 nm, respectively, and attains a large critical field of $H_x \approx 20$ kOe for $d = 36$ nm, which are indicated by the arrows in Fig. 3(d). On the contrary, for continuous Nb thin film, only the flux-creep dominant regime was observed as shown in Fig. 3(d) (star symbols). We remark that the reduction of $\Delta T_c/T_c$ is only sensitive to the field component that is perpendicular to the INHL [22], which excludes the extrinsic disorder effects.

In a Nb thin film with thickness of about 30 nm, the zero temperature superconducting coherent length ξ_0 and penetration depth $\lambda(0)$ are both around 100 nm [27]. In our continuous Nb film with $t = 34$ nm shown in Fig. 1(c), the residual resistivity $\rho_0 \approx 7.1\,\mu\Omega\,\mathrm{cm}$ with $T_c = 8.2$ K agrees with the thickness dependence of ρ_0 and T_c reported previously in sputtered Nb thin films [27]. Using the phenomenological value of $\rho_0\ell = 3.72 \times 10^{-6}\,\mu\Omega\,\mathrm{cm}^2$ [27,28], we deduced a mean free path $\ell \approx 5$ nm in our continuous Nb thin film, giving the ratio of ξ_0/ℓ about 20. The effective superconducting coherence length can then be described by $\xi(T) \approx (\xi_0\ell)^{1/2}/(1 - T/T_{c0})^{1/2}$ in the dirty limit [4], where T_{c0} is the BCS superconducting transition temperature. Therefore, the $\xi(T) \geqslant \xi(0) \approx (\xi_0\ell)^{1/2} \approx 23$ nm, and it grows larger when approaching T_c. As shown in Fig. 3(d), within the resistive transition range, maximum $\Delta T_c/T_c$ equals 0.22 (0.01) giving a lower limit of the coherent length $\xi(T) \approx 50$ nm (200 nm) for $d = 36$ nm (89 nm), which justifies the quasi-1D limit for the observed phenomena in our sub-100 nm INHLs. The suppression of T_c is then intimately related to thermally activated phase slips in the nanoconstriction, which gives rise to a reduced phase rigidity in INHL compared to a continuous Nb thin film. INHL thus shows close resemblance to a high-T_c superconducting cuprate system in terms of weak phase rigidity. The suppression of transition width under magnetic field in INHL shown in Fig. 3(c) is reminiscent of the vortex-liquid to vortex-solid transition in cuprates [29]. At low fields, the flux lines form a liquid phase and can hop across each other within the INHL resulting in large phase fluctuations and hence a broad transition width. Due to the repelling nature of the flux lines, the maximum number of flux lines within each cell can be calculated using $n_s = D/4\xi(T)$ [30,31], where D is the diameter of the cell. In our INHLs, we estimate $n_s \leqslant 2$. As the field increases to above the critical field H_x, the number of flux lines within each cell already saturated making it energetically unfavorable for the flux lines to move around. This collective flux-line pinning effect [32,33] strongly reduces the phase fluctuations in INHLs and makes the transition width narrower in higher magnetic fields. The resulting phase diagram of the flux-line lattice is shown in Fig. 4, where a phase transition between liquid (lower-left

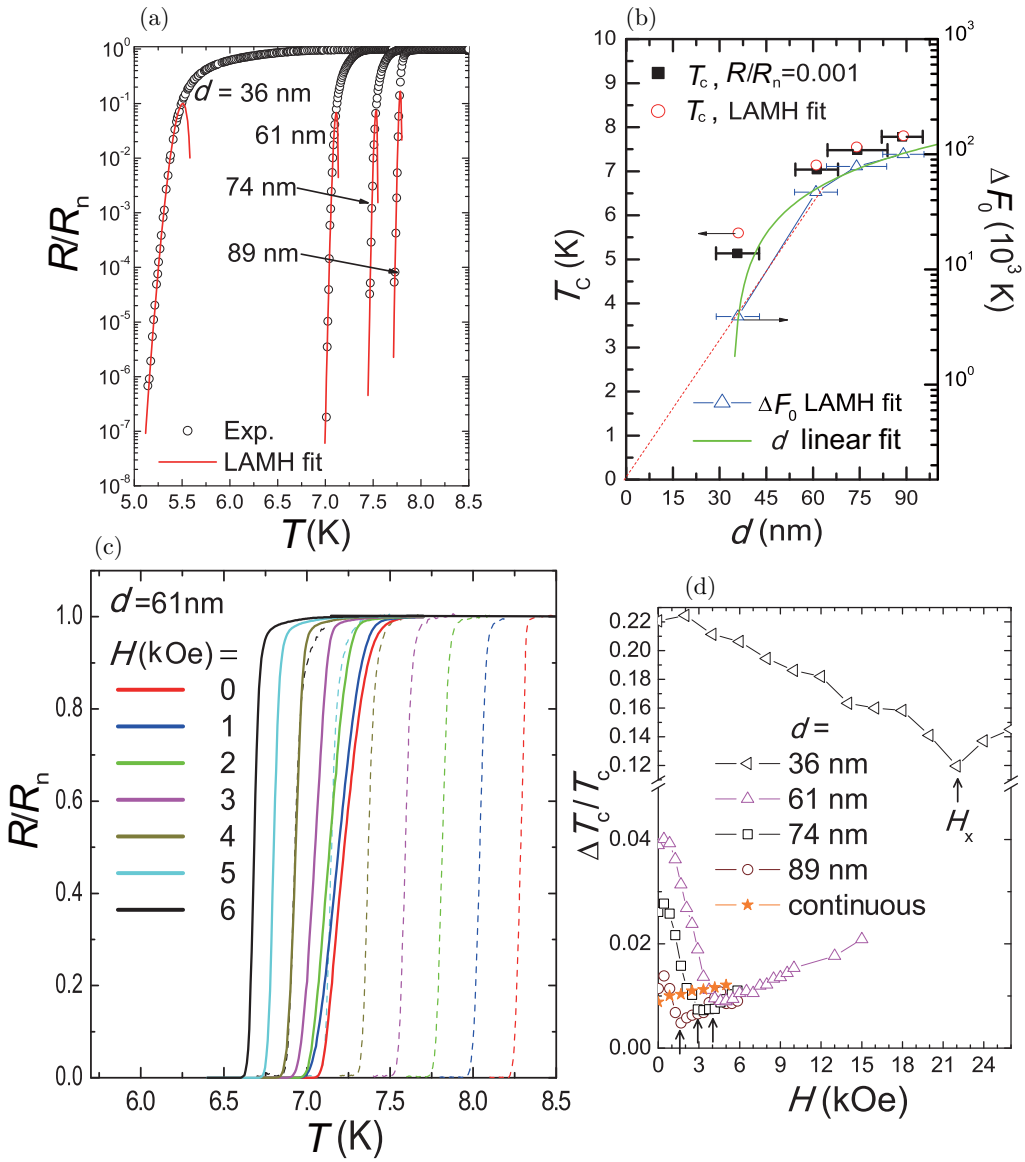

FIG. 3. (a) LAMH fittings (red lines) to the R/R_n-T curves in four INHL samples with difference d's under investigation. (b) The d dependence of the two fitting parameters: T_c and zero-temperature free energy barrier ΔF_0, obtained from LAMH model. The solid squares are the T_c values obtained from the resistance data with $R/R_n = 0.001$. ΔF_0 is practically linear with d, but it appears to exponentially decay with d as $d \leqslant 60$ nm. (c) R/R_n-T curves under perpendicular magnetic fields H. The solid and dotted lines are the data for $d = 61$ nm and continuous Nb thin film, which shares the same color codes representing different H values ranging from zero to 6 kOe. For $d = 61$ nm, the superconducting transition width apparently decreases with increasing H, which is in big contrast to the continuous Nb thin film that shows little variation of transition width with H. (d) The normalized transition width $\Delta T_c/T_c$ versus H. A rapid decrease of $\Delta T_c/T_c$ with increasing H appears in all INHL samples, where it reaches a local minimum at the critical field H_x. H_x values, indicated by the black arrows, are strongly d-dependent and grow larger for smaller d.

image of Fig. 4) to solid (upper-right image of Fig. 4) can be driven by tuning either the phase-slip junction width d or external magnetic field. We remark that such behavior is absent in the single superconducting nanowire system that shows no apparent change in the transition width under field [34].

The broadening of resistive transition in zero field can also arise from the dissociation of vortex-antivortex pairs [17,18,35,36]. For $T \geqslant T_{\mathrm{BKT}}$, a finite resistance appears due to increasing population of unbounded vortices, which follows a special T dependence of $R_\square = R_0 \exp[-b(T/T_{\mathrm{BKT}} - 1)^{-1/2}]$. This, however, was not observed in our continuous Nb films and INHL samples [22]. We also note that the sheet resistance in our samples ($2\Omega \leqslant R_\square \leqslant 53.4\Omega$) is more than two orders of magnitude smaller than those superconducting films showing BKT transition. In addition, the nanoconstriction width in our INHL samples (36 nm $\leqslant d \leqslant$ 89 nm) and the distance between the superconducting islands ($a \cong 200$ nm) are merely at similar length scale as the superconducting coherence length $\xi(T)$, which makes our INHL different from the regular superconducting arrays with weak links and a sizable junction coupling energy. We, therefore, argue that the BKT

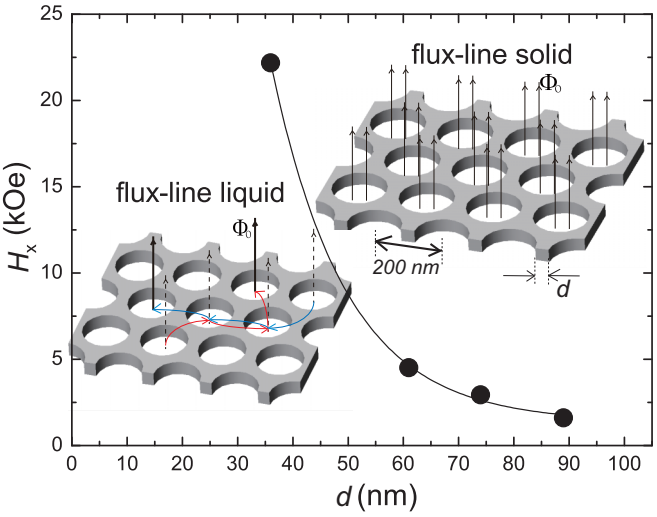

FIG. 4. Critical field H_x versus d that separates two distinct phases of flux lines. In liquid phase, the flux lines can move around within the INHL and cross each other without costing much energy as illustrated in the lower-left image. Large phase fluctuations can appear in the liquid phase. On the contrary, as H increases, the collective pinning effect drives the flux lines into a solid phase, where flux lines are mostly pinned either inside the cell or within the INHL, and thus the phase fluctuations are strongly suppressed.

type transition is unlikely to be important in our INHL samples.

In summary, we have demonstrated the feasibility of reducing the phase rigidity in a superconductor via artificial nanostructures. This is strongly supported by the observation of a wide superconducting transition width in zero field that can be well-fitted to the thermally activated phase-slips model. We also uncovered an unusual reduction of transition width with increasing magnetic field, which can be understood in terms of a magnetic-field-driven phase transition from a flux-line liquid phase into a solid phase in INHL due to collective pinning effect. This behavior is consistent with the scenario of reduced phase rigidity in INHL via interconnected phase-slip junctions, where an intriguing vortex-liquid state can be realized in a conventional low-T_c superconductor with artificial nanostructures. Our work provides an important experimental advancement to the phenomena associated with the phase fluctuations in superconducting nanostructures.

The authors acknowledge the funding support from Ministry of Science and Technology in Taiwan and also technical support from Core Facility for Nanoscience and Nanotechnology at Academia Sinica in Taiwan. We are grateful to C. C. Chi, J. Clarke, H.-M. Cho, N. P. Ong, I. Bozovic, and W. Wu for fruitful discussions.

[1] Z. A. Xu, N. P. Ong, Y. Wang, T. Kakeshita, and S. Uchida, Nature (London) **406**, 486 (2000).
[2] Y. Wang, L. Li, and N. P. Ong, Phys. Rev. B **73**, 024510 (2006).
[3] L. Li, J. G. Checkelsky, S. Komiya, Y. Ando, and N. P. Ong, Nat. Phys. **3**, 311 (2007).
[4] *Introduction to Superconductivity*, edited by M. Tinkham (Dover Publications, New York, 1996).
[5] *Superconductivity of Metals and Alloys*, edited by P. de Gennes (Addison-Wesley, New York, 1966).
[6] C. N. Lau, N. Markovic, M. Bockrath, A. Bezryadin, and M. Tinkham, Phys. Rev. Lett. **87**, 217003 (2001).
[7] A. Rogachev and A. Bezryadin, Appl. Phys. Lett. **83**, 512 (2003).
[8] V. L. Berezinskii, Zh. Eksp. Teor. Fiz. **59**, 907 (1970) [Sov. Phys. JETP **32**, 493 (1971)].
[9] V. L. Berezinskii, Zh. Eksp. Teor. Fiz. **61**, 1144 (1971) [Sov. Phys. JETP **34**, 610 (1972)].
[10] J. M. Kosterlitz and D. J. Thouless, J. Phys. C **5**, L124 (1972).
[11] W. A. Little and R. D. Parks, Phys. Rev. Lett. **9**, 9 (1962).
[12] B. Pannetier, J. Chaussy, R. Rammal, and J. C. Villegier, Phys. Rev. Lett. **53**, 1845 (1984).
[13] M. Baert, V. V. Metlushko, R. Jonckheere, V. V. Moshchalkov, and Y. Bruynseraede, Phys. Rev. Lett. **74**, 3269 (1995).
[14] U. Welp, Z. L. Xiao, J. S. Jiang, V. K. Vlasko-Vlasov, S. D. Bader, G. W. Crabtree, J. Liang, H. Chik, and J. M. Xu, Phys. Rev. B **66**, 212507 (2002).
[15] U. Patel, Z. L. Xiao, J. Hua, T. Xu, D. Rosenmann, V. Novosad, J. Pearson, U. Welp, W. K. Kwok, and G. W. Crabtree, Phys. Rev. B **76**, 020508(R) (2007).
[16] I. Sochnikov, A. Shaulov, Y. Yeshurun, G. Logvenov, and I. Božović, Nat. Nanotechnol. **5**, 516 (2011).
[17] M. R. Beasley, J. E. Mooij, and T. P. Orlando, Phys. Rev. Lett. **42**, 1165 (1979).
[18] H. S. J. van der Zant, H. A. Rijken, and J. E. Mooij, J. Low Temp. Phys. **79**, 289 (1990).
[19] M. D. Stewart, Jr., A. Yin, J. M. Xu, and J. M. Valles, Jr., Science **318**, 1273 (2007).
[20] A. Bezryadin and P. M. Goldbart, Adv. Mater. **22**, 1111 (2010).
[21] C.-C. Ho, P.-Y. Chen, K.-H. Lin, W.-T. Juan, and W.-L. Lee, ACS Appl. Mater. Interfaces **3**, 204 (2011).
[22] See Supplemental Material at http://link.aps.org/supplemental/10.1103/PhysRevB.96.020506 for more details on the nanostructure characterizations, magneto-transport data at different field orientations, and BKT transition fittings.
[23] J. S. Langer and V. Ambegaokar, Phys. Rev. **164**, 498 (1967).
[24] D. E. McCumber and B. I. Halperin, Phys. Rev. B **1**, 1054 (1970).
[25] M. Vanević and Y. V. Nazarov, Phys. Rev. Lett. **108**, 187002 (2012).
[26] P. W. Anderson and Y. B. Kim, Rev. Mod. Phys. **36**, 39 (1964).
[27] A. I. Gubin, K. S. Il'in, S. A. Vitusevich, M. Siegel, and N. Klein, Phys. Rev. B **72**, 064503 (2005).
[28] T. R. Lemberger, I. Hetel, J. W. Knepper, and F. Y. Yang, Phys. Rev. B **76**, 094515 (2007).
[29] W. K. Kwok, S. Fleshler, U. Welp, V. M. Vinokur, J. Downey, G. W. Crabtree, and M. M. Miller, Phys. Rev. Lett. **69**, 3370 (1992).
[30] G. Mkrtchyan and V. Shmidt, Zh. Eksp. Teor. Fiz. **61**, 367 (1971) [Sov. Phys. JETP **34**, 195 (1972)].

[31] V. V. Moshchalkov, M. Baert, V. V. Metlushko, E. Rosseel, M. J. Van Bael, K. Temst, Y. Bruynseraede, and R. Jonckheere, Phys. Rev. B **57**, 3615 (1998).

[32] A. I. Larkin and Y. N. Ovchinnikov, J. Low Temp. Phys. **34**, 409 (1979).

[33] L. Krusin-Elbaum, L. Civale, V. M. Vinokur, and F. Holtzberg, Phys. Rev. Lett. **69**, 2280 (1992).

[34] A. Rogachev, A. T. Bollinger, and A. Bezryadin, Phys. Rev. Lett. **94**, 017004 (2005).

[35] A. T. Fiory, A. F. Hebard, and W. I. Glaberson, Phys. Rev. B **28**, 5075 (1983).

[36] C. J. Lobb, D. W. Abraham, and M. Tinkham, Phys. Rev. B **27**, 150 (1983).